Combining IR and X-ray microtomography data sets: application to Itokawa particles and to Paris meteorite

Zelia Dionnet, Rosario Brunetto, Alice Aleon-Toppani, Stefano Rubino, Donia Baklouti, Ferenc Borondics, Anne-Cécile Buellet, Zahia Djouadi, Andrew King, Tomoki Nakamura, et al.

The Meteoritical Society

Meteoritics & Planetary Science 55, Nr 7, 1645–1664 (2020)
doi: 10.1111/maps.13538

Combining IR and X-ray microtomography data sets: Application to Itokawa particles and to Paris meteorite

Zelia DIONNET[1,2]*, Rosario BRUNETTO[3], Alice ALÉON-TOPPANI[3], Stefano RUBINO[3,4], Donia BAKLOUTI[3], Ferenc BORONDICS[4], Anne-Cécile BUELLET[5], Zahia DJOUADI[3], Andrew KING[4], Tomoki NAKAMURA[6], Alessandra ROTUNDI[1,2], Christophe SANDT[4], David TROADEC[7], and Akira TSUCHIYAMA[8,9]

[1]DIST-Università Parthenope, Napoli, Italy
[2]INAF-IAPS, Roma, Italy
[3]Institut d'Astrophysique Spatiale, CNRS, Université Paris-Saclay, Orsay, France
[4]SOLEIL synchrotron, Gif-sur-Yvette, France
[5]Université Paris Saclay, Orsay, France
[6]Division of Earth and Planetary Materials Science, Laboratory for Early Solar System Evolution, Tohoku University, Sendai, Japan
[7]Institut d'Electronique, de Microélectronique et de Nanotechnologie, Villeneuve d'Ascq, France
[8]Research Organization of Science and Technology, Ritsumeikan University, Kyoto, Japan
[9]Guangzhou Institute of Geochemistry, Guangdong, China
*Corresponding author. E-mail: zelia.dionnet@uniparthenope.it

(Received 03 May 2019; revision accepted 26 May 2020)

Abstract–In the near future, a new generation of sample return missions (Hayabusa2, OSIRIS-REx, MMX, etc.) will collect samples from small solar system bodies. To maximize the scientific outcome of laboratory studies and minimize the loss of precious extraterrestrial samples, an analytical sequence from less destructive to more destructive techniques needs to be established. In this work, we present a combined X-ray and IR microtomography applied to five Itokawa particles and one fragment of the primitive carbonaceous chondrite Paris. We show that this analytical approach is able to provide a 3-D physical and chemical characterization of individual extraterrestrial particles, using the measurement of their 3-D structure and porosity, and the detection of mineral and organic phases, and their spatial co-localization in 3-D. We propose these techniques as an efficient first step in a multitechnique analytical sequence on microscopic samples collected by space missions.

INTRODUCTION

In the study of the origin and evolution of the solar system, many questions about the physicochemical processes that have affected solid materials in the solar nebula and in the planetesimals are still open (Flynn et al. 2016). The laboratory analyses of extraterrestrial samples from small solar system bodies (asteroids, comets) provide valuable information as they give a direct access to the compositional heterogeneity resulting from these processes (Rietmeijer 1998; Alexander et al. 2007).

In this context, sample return missions such as Stardust (NASA) from comet Wild 2 (Brownlee et al. 2006) and Hayabusa (JAXA) from S-type asteroid Itokawa (Abe et al. 2006) provided a particularly significant contribution, as they allowed an unequivocal link between the laboratory samples and their parent bodies, which is rarely the case for meteorites and interplanetary dust particles (IDPs). A new generation of sample return missions is collecting samples from possibly carbon-rich small asteroids: Hayabusa2 (JAXA) from C-type asteroid Ryugu (Takagi et al. 2011; Kitazato et al. 2019; Sugita et al. 2019; Watanabe et al. 2019) and OSIRIS-REx (NASA) from B-type asteroid Bennu (Lauretta et al. 2015). More sample return missions are planned for the near future, such as MMX (JAXA) which will retrieve samples from the Martian moon Phobos (Campagnola et al. 2018).

Given the limited amount of material that is usually retrieved by all these sample return missions, optimizing the analytical strategy in order to maximize the scientific outcome and minimize the sample loss is also a significant challenge for the laboratory community. In fact, while the heterogeneity of extraterrestrial materials can be efficiently investigated by different techniques such as scanning or transmission electron microscopy (SEM and TEM, e.g., Bradley et al. 1992; Le Guillou et al. 2014), nanoscale secondary ion mass spectrometry (nanoSIMS, e.g., Hoppe 2006), and X-ray absorption near edge structure spectroscopy (XANES, e.g., Cody et al. 2008; Vinogradoff et al. 2017), each technique has its intrinsic detection biases and they are all destructive to some extent or imply a sample preparation with significant loss of material (e.g., sectioning). Recently, new measurements of micro-Raman spectroscopy have been performed to allow 3-D Raman tomography (Yesiltas et al. 2018), but so far very few techniques can give us chemical information and still preserve the chemical and structural integrity of the sample. The necessity to develop a sequence of laboratory analyses combining different techniques for a complete characterization of the extraterrestrial materials is a major issue (Nakamura et al. 2014). It is clear that 3-D nondestructive analyses play a crucial role in such sequences: for instance, X-ray microtomography (or X-CT for X-ray computed tomography) was applied as one of the first techniques on a few Itokawa particles (Nakamura et al. 2011; Tsuchiyama et al. 2011), and on Stardust samples (Nakamura et al. 2008; Tsuchiyama et al. 2009).

Among these techniques, infrared (IR) imaging microspectroscopy (e.g., Yesiltas et al. 2014) is a suitable tool as it is totally nondestructive. It is able to characterize molecular vibrations and phonons, and in particular to detect both mineral and carbonaceous phases that are commonly observed in extraterrestrial materials such as primitive meteorites (e.g., Pendleton et al. 1994; Merouane et al. 2012) or IDPs (e.g., Merouane et al. 2014). It is also able to map the spatial distribution of different components (with spatial resolutions that are limited by the mid-IR photon wavelengths, typically 2–15 μm) and their assembly and thus to get constraints about their formation and their evolution in the young solar system (e.g., Dionnet et al. 2018a). Its sensitivity to -O-H vibrations allows one to study the hydration of extra-terrestrial samples. Last but not least, laboratory IR spectroscopy allows comparison with astronomical observations of small solar system bodies (asteroids, comets, trans-Neptunian objects; e.g., Brunetto et al. 2011).

Thanks to the recent developments of Fourier transform (FT) IR hyperspectral imaging setups, in particular those using focal plane array (FPA) detectors, FT-IR microtomography has become possible (Martin et al. 2013). This technique has been applied on geological and biological samples (Martin et al. [2013] with a synchrotron source and Quaroni et al. [2015] with a globar source) as well as on one fragment of the Murchison meteorite (Yesiltas et al. 2016). IR tomography could be performed on samples with a size between 10 and 60 μm (limited by signal saturation).

In view of the next sample return missions from asteroids Ryugu and Bennu, the goals of this work are to implement a dedicated setup for 3-D FTIR hyperspectral imaging and for the first time to combine IR and X-ray microtomography analyses on extra-terrestrial particles. We have chosen five grains from asteroid Itokawa, as a case for extraterrestrial materials collected by sample return missions and one grain from the Paris meteorite, as an example of a carbonaceous extraterrestrial sample. In the following, we illustrate how the two techniques together surmount the intrinsic limitations of each one, giving access to the identification and spatial distribution of both organic and mineral components inside the analyzed particles, as well as their 3-D structure and porosity.

MATERIALS AND METHODS

Sample Description and X-Ray Analyses

Itokawa's Particles

The first set of extraterrestrial samples analyzed in this work are particles from asteroid Itokawa, collected by the Hayabusa mission and brought back to Earth in 2010 (Yoshikawa et al. 2007). We received five particles from JAXA: RA-QD02-0214 (36 μm size), RA-QD02-0223 (54 μm), RA-QD02-0232 (38 μm), RA-QD02-0156 (37 μm), and RB-QD04-0046 (42 μm). Four particles came from room A and one from room B of the Hayabusa sample container (Yano et al. 2006; Yada et al. 2014). The SEM-EDX measurements included in the JAXA Hayabusa sample catalog for these five particles indicate the presence of olivine, plagioclase, Ca-rich pyroxene, Ca-poor pyroxene, and troilite.

In 2014, these particles have been mounted at the extremity of individual carbon fibers by using an epoxy glue (preparation by T. Nakamura, see supplementary online material in Tsuchiyama et al. 2011) as shown in Fig. 1a. The use of the epoxy glue to fix the particles on the fibers implied a contamination by organics. We will later see that this issue turned out to be an opportunity in our case, to test and improve our 3-D tomography reconstruction, separating asteroid minerals from the organic contaminants.

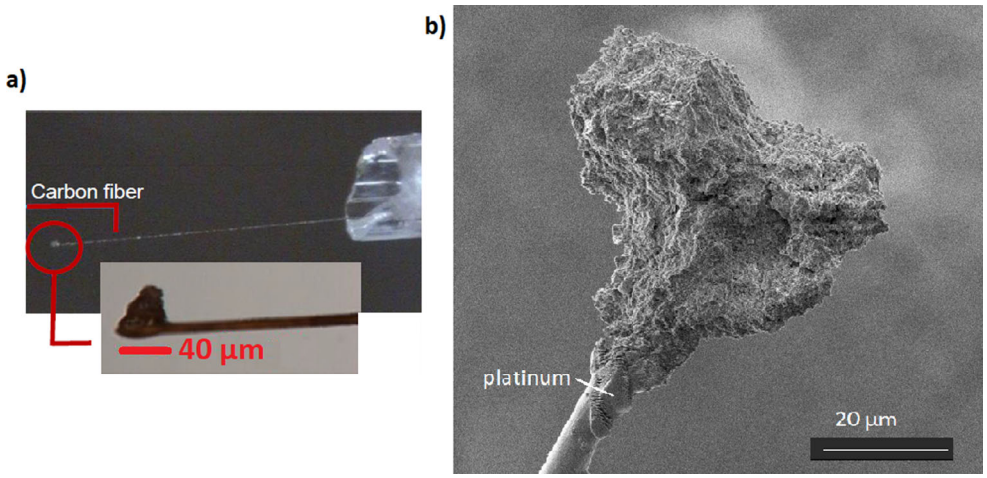

Fig. 1. a) Preparation of the asteroid samples RA-QD02-0223 at JAXA, fixed with epoxy at the end of a carbon fiber. b) Preparation of the Paris meteorite welded with platinum at the end of a tungsten needle. (Color figure can be viewed at wile yonlinelibrary.com.)

A precise identification of the minerals of these particles was performed by the team of T. Nakamura, using synchrotron X-ray diffraction (see Nakamura et al. [2011] for more details on the experimental setup and procedure). The abundance of each mineral and its 3-D distribution was obtained by X-CT, with a spatial resolution of ~200 nm (details of the technique and setup in Tsuchiyama et al. 2013). The X-ray data used in this work were collected at beamline BL47XU in SPring-8, Japan (see Tsuchiyama et al. [2011, 2014] for technical details), with a flux of 2.05×10^{11} phs s^{-1} mm^{-2} for the measurement at 7 keV and 3.57×10^{11} phs s^{-1} mm^{-2} for the one at 8 keV. To precisely determine the composition and to distinguish between different minerals such as low-Ca pyroxene and olivine with different Fe contents, tomography measurements at 7 and 8 keV are combined, respectively, below and above the K absorption edge of Fe (7.11 keV). Differences are then observed in the linear attenuation coefficient (LAC) according to the concentration of iron. Minerals with elements heavier than Si but lighter than Fe have relatively large LAC values at 7 keV, while Fe-rich minerals have large LAC values at 8 keV.

Particle from the Paris Meteorite

We also analyzed a particle, with a diameter of 40 µm, extracted from the matrix of the Paris meteorite, a very primitive CM chondrite (Zanda et al. 2010; Hewins et al. 2014). This particle was welded with platinum at the extremity of a tungsten needle using a focused ion beam (see Fig. 1b). We first performed IR tomography on this sample at the SMIS beamline of SOLEIL (see below) and then X-CT measurements at the PSICHE beamline of SOLEIL (France) with an energy of 17.6 keV and a photon flux of 1.6×10^{11} phs s^{-1} mm^{-2}. This campaign of measurement was done at only one energy. This does not allow us to clearly identify the minerals present in the sample, as opposed to the case of the measurements performed on SPring-8 for Itokawa's particles. In the case of the Paris meteorite, we used X-ray data to study the porosity and characterize the assemblage of components at the micron scale. Moreover, it was useful to extract the precise shape of the sample and therefore constrain the IR data.

IR Microtomography

We analyzed the five Itokawa particles and the Paris particle using the same IR microtomography setup. FTIR data were collected after the X-ray data, using an Agilent Cary 670/620 microspectrometer installed at the SMIS beamline of the SOLEIL synchrotron in France. We worked with its internal Globar source in transmission mode and used 25× objective and condenser (numerical aperture 0.81) coupled with high magnification optics (providing an additional 2.5× magnification increase) placed in front of a 128 × 128 pixels FPA detector. In this way, we obtained a projected pixel size of about 0.66 µm on the focal plane, and a field of view of about 84 µm. We collected hyperspectral data, that is, for each pixel, we obtained a whole IR spectrum in the 850–3950 cm^{-1} spectral range. The spatial resolution (between 2.5 and 15 µm) was diffraction limited for the whole investigated IR spectral range. Even if the resolution obtained with FT-IR microtomography is not as good as the one obtained with X-CT (because of the diffraction in the IR range), FT-IR has the advantage

of being able to detect and precisely identify the organic components.

As the samples were fixed at the end of carbon fibers or a tungsten needle, we used a mandrel to hold the needles horizontally. This mandrel was connected to a small kinematic adjustable mount which was itself connected to a motor to rotate the sample on the focal plane of the objective. All this setup was fixed to the X–Y stage of the microscope (see Fig. 2). For each sample, we collected a 2-D hyperspectral map in transmission for each rotation angle. We call this measurement a 2-D hyperspectral projection. A typical IR microtomography acquisition consisted of 180 measured hyperspectral projections. A complete IR microtomography data set thus consisted of about three million spectra ($128 \times 128 \times 180$). At every projection, the sample was rotated by one degree, and its X–Y–Z position was adjusted manually to always keep it at the focal plane and at the center of the projected FPA matrix. We accumulated and averaged 32 scans for each projection, and the spectral resolution was 16 cm^{-1}. The center of the sample could move of few pixels during the whole rotation. Postmeasurement correction was performed by adjusting the position of the needle between the different projections, and we estimated that these induced reconstruction artifacts were minimal.

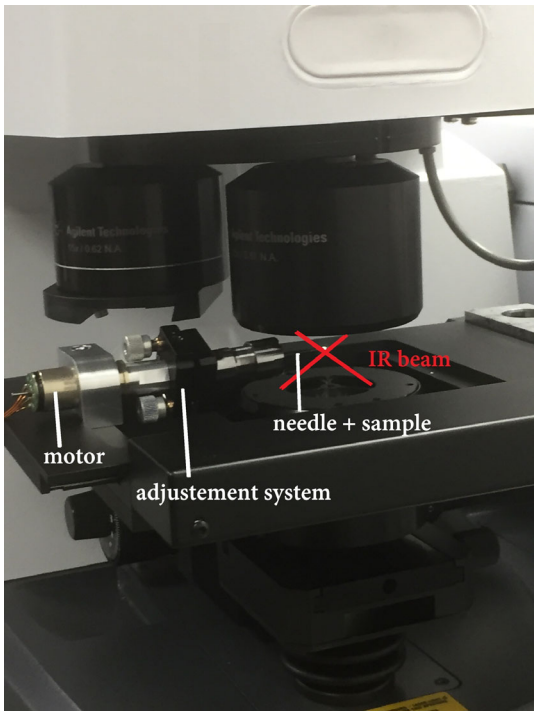

Fig. 2. Picture of the IR tomography setup, with the needle and sample mounted on the focal plane of the 25× objective. The motor allows us to perform 360 rotations of the sample in the focal plan. (Color figure can be viewed at wileyonlinelibrary.com.)

2-D Projected Maps of Functional Groups

The molecular components present in the samples were identified by assigning the absorption bands observed in the average IR spectra. The average IR spectrum of each sample was obtained by averaging all pixels in all the projections which contain a significant amount of material (a filter of 10% was applied based on the intensity of the absorbance at the 2.8 μm wavelength). For each sample, the number of pixels in all projections with a significant amount of material varies between 300,000 and 400,000 (depending on the size of the sample). In some cases (reconstruction of the different minerals), it was also possible to identify molecular components by using second derivatives of the spectra (Susi and Byler 1983), a method allowing us to partly remove the bias of the underlying IR continuum. The components that we identified in our samples are given in Table 1.

The 2-D projected maps of the functional groups were generated using the following steps. First, we divided each acquisition by the background collected without the sample. For each spectrum in each projection measured at a given angle, we extracted the projected abundance (column density, oscillators.cm^{-2}) of the different functional groups associated with specific absorption bands (see Table 1) by calculating the area under the corresponding band in the IR spectra or by considering the intensity of the second derivative. We used the following range for the integration under the band: OH (3216 to 3526 cm^{-1} with a larger baseline between 2646 and 3674 cm^{-1}), organics (2814–2955 cm^{-1} with a larger baseline between 2778 and 2999 cm^{-1}), and carbonates (1445–1476 cm^{-1} with a larger baseline between 1330 and 1551 cm^{-1}). We thus obtained a map of column density at the considered angle, and repeated the calculation for all angles, creating a set of 2-D projected maps for each functional group detected in the samples. All maps were then normalized to the maximum value of column density found in the whole data set for that specific IR band. This last operation resulted in a set of pictures in RGB scale where the minimum value of normalized intensity (in blue) corresponds to an absence of this component and the maximum value (in red) corresponds to pixels with the highest concentration of this component (see Figs. 5 and 6).

Reconstruction and 3-D Data Analysis

We used TXM-Wizard, a software developed and described by Liu et al. (2011, 2016), to reconstruct the 3-D spatial distribution of the different components starting from the 2-D projections. The algorithm used

Table 1. List and attribution of the main IR spectral signatures in the five Itokawa samples.

Frequency (cm^{-1})	Attribution	Samples				
		0214	0223	0232	0156	0046
Extra-terrestrial material						
1140–850	υ Si-O of silicates	x	x	x	x	x
971	υ Si-O of an olivine	x			x	x
1018–1025	υ Si-O calcium-poor pyroxene		x	x		
1049	υ Si-O calcium-rich pyroxene	x				
1180	υ S-O of a sulfate	x	x	x	x	x
Glue						
1110	C-O	x	x	x	x	x
1249	CC aromatic skeleton	x	x	x	x	x
1373	δ CH_2 deformation	x	x	x	x	
1450	δ CH	x	x	x	x	
1570–1774	δ OH	x	x	x	x	x
1604	υ C = C aromatic	x	x	x	x	x
1690–1790	υ C = O (COO conjugated ester)	x	x	x	x	x
2864	υ CH_3 symmetric	x	x	x	x	x
2962	υ CH_3 asymmetric	x	x	x	x	x
3062	υ CH aromatic	x	x	x	x	x
3000–3750	υ OH	x	x	x	x	x

Particles (δ is used to describe bending vibrations and υ for stretching vibrations). The bands were attributed based on Yesiltas et al. (2014) and Beck et al. (2014) for the mineral bands, and Dartois et al. (2005) for the organic bands.

was the iterative algebraic reconstruction technique (ART) with 20 iterations (beyond 20 iterations, the quality of the reconstructed images did not improve significantly). After execution, TXM-Wizard also provided a new set of images representing slices inside the sample for the three planes (x, y), (x, z), (y, z). We obtained voxels with a size corresponding to the size of pixels in the measured projections, that is, 0.66 μm. Finally, we used the Avizo software to visualize the position of each phase in 3-D and investigate the spatial distribution and co-localization of the different phases. To quantify the co-localization of the two chemical phases, we estimated the Pearson product moment, which measures the linear correlation between two data sets. A value around zero means no spatial relation between the chosen distributions, while a value above 0.8 is considered as the sign of a co-localization.

The estimation of the CH oscillators per voxel was calculated from the reconstructed 3-D spatial distribution of the area of the aliphatic band (2814 to 2955 cm^{-1}). After a normalization by voxel size, we used the band strengths A in each voxel (see value in Dionnet et al. 2018a), to deduce the column density N (molecules cm^{-3}) using the following formula: N = Area/A.

Superposition of the IR and X Data Sets

The last step was to superimpose IR and X microtomography data sets. Since these two data sets have different spatial samplings (voxel size of X-ray measurements is 0.073 μm in the case of Itokawa samples and 0.13 μm in the case of Paris meteorite, versus 0.66 μm in the case of all IR measurements), we first had to downsample the X-ray data by averaging nine (for Itokawa samples) and five (for Paris sample) X-ray voxels in each spatial direction.

The two measurements were performed on different setups with different orientations of the reconstructed samples. Thus, in order to combine the two data sets, we adjusted the spatial position and orientation of the X-ray 3-D data set to the IR 3-D data set. To achieve this, we first reconstructed in 3-D the absorbance value of the IR continuum at 2.8 μm (3570 cm^{-1}). Absorption and scattering producing the IR continuum are very sensitive to the whole quantity of matter probed by the IR beam and the 2.8 μm wavelength provides the best trade-off between spatial resolution and signal to noise ratio in our IR range (the diffraction effect is stronger for higher wavelength such as those around 10 μm used to retrieve the silicate distribution). Therefore, reconstructing in 3-D the IR continuum allowed us to quickly visualize the volume of the whole sample and its needle. We then adjusted the spatial offset position and orientation of X-CT data set to match as best as possible the 3-D reconstructed IR continuum. A first rough adjustment was obtained by matching the needle's position. Finally, to perform a more precise adjustment, we varied six spatial parameters (three rotations and three translations) and

we maximized the spatial correlation coefficient (around 0.85 after optimization) between the 3-D X-ray LAC and the 3-D IR continuum at 2.8 μm.

Shape Model Obtained from X-Ray Data

A major advantage of the combination of the two data sets was the possibility to use the better spatial resolution of the X-ray data to constrain the shape of the IR reconstruction and to partially counterbalance the scattering/diffraction effects on IR data. At the scale of these samples, diffraction effects are important in the IR range and thus lead to a blurring (low spatial resolution) of the data. We used the 3-D distribution of the LAC obtained with X-CT to create a shape model to delimit the contour of the sample and the edges between different phases with a higher resolution. To define this shape model, we relied on levels of gray. An example is provided in Fig. 3, where the points with intensity lower than 5 represent the empty space around the sample and their signal is a combination of intrinsic noise due to the X-ray measurement and of uncertainties due to the reconstruction algorithm. Values between 5 and 35 (see green boxes in Figs. 3b and 3c) are found to be characteristic of the glue and the needle, which have low X-ray absorption. Values in the range 100–170 (see red box Fig. 3c) typically correspond to the mineral phases present in the extra-terrestrial particles.

By keeping only the voxels corresponding to the sample, we defined a contour for the sample and we applied it as a spatial filter to the IR data. In this way, we better constrained the shape of the IR-reconstructed sample and removed spurious IR voxels polluted by diffraction and diffusion.

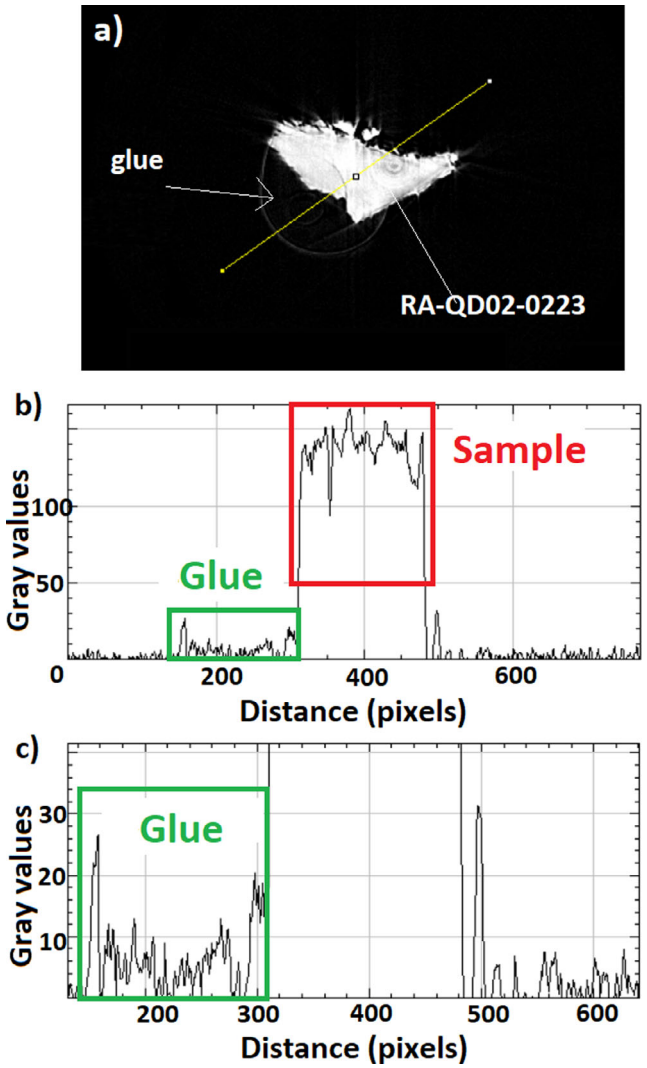

Fig. 3. a) Slice (xy) of the 3-D X-ray reconstructed particle RA-QD02-0214, (b) LAC profile along the yellow line of (a), (c) zoom of the LAC profile for small values. The rectangles show typical filters used to isolate the glue from the extra-terrestrial particle and to create the X-ray shape model. (Color figure can be viewed at wileyonlinelibrary.com.)

RESULTS

Itokawa's Particles

Results of X-CT data allowed us to classify the five particles according to their heterogeneity in mineral phases. A first kind of particles (RA-QD02-0156, RB-QD04-0046, and RA-QD02-0223) were largely dominated by one mineral component according to X-ray measurements, see Fig. 4a. A second kind of sample was particle RA-QD02-0214, composed of two spatially well-separated mineral phases. Panel (b) of Fig. 4 shows a slice of this particle, with olivine on the left and the Ca-rich pyroxene on the right. Finally, particle RA-QD02-232 showed a more complex structure with a higher heterogeneity (see Fig. 4c). We observed small inclusions of troilite (FeS, noted as Tr), chromite ($FeCr_2O_4$, noted as Cm), and taenite (FeNi) inside a Ca-poor pyroxene.

The IR data partially confirmed the silicate identification. Table 1 lists the peak positions of the bands observed in the spectra of the five Itokawa samples. In each point where there is silicate according to the X-ray data, we detected a broad band between 850 and 1140 cm^{-1}. Using dual-energy X-CT, we have a more precise identification, and thus, we checked the presence of small silicate features, as the shape and the peak position of these bands varied according to the presence of different mineral features (see Fig. 5b). For instance, a maximum around 1049 cm^{-1} revealed the presence of Ca-rich pyroxene while a maximum at 971 cm^{-1} was characteristic of the presence of a $Fo_{65\pm 5}$

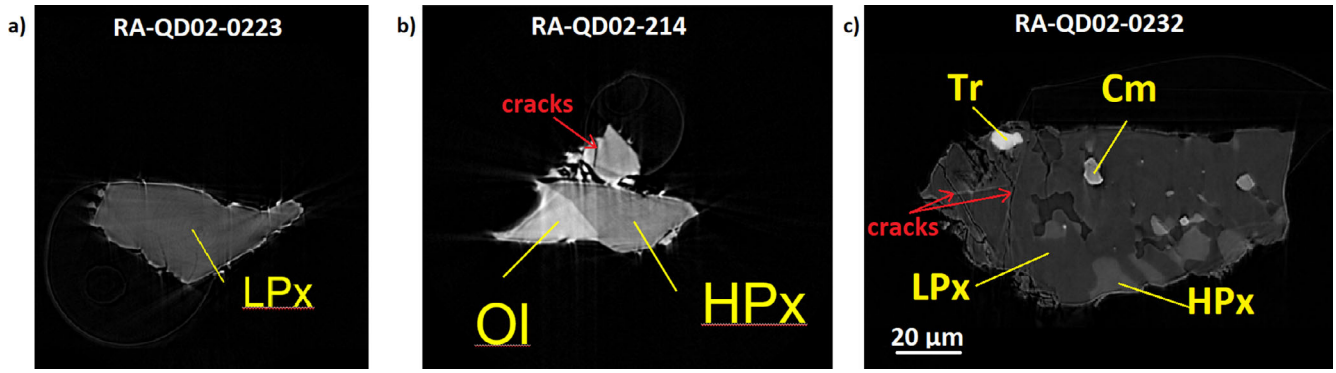

Fig. 4. X-ray (xy) slices measured at 7 keV for (a) RA-QD02-0223, (b) RA-QD02-0214, and (c) RA-QD02-0232 with the following abbreviations: LPx for low-calcium pyroxene, Ol for olivine, HPx for high-calcium pyroxene, Tr for troilite, and Cm for chromite. (Color figure can be viewed at wileyonlinelibrary.com.)

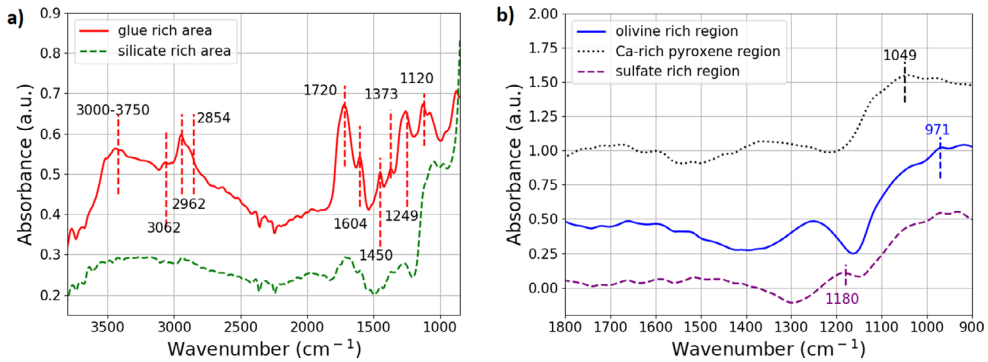

Fig. 5. a) Example of typical spectra, before reconstruction, mainly representative of glue (red) and minerals (green) for one projection of particle RA-QD02-0214. b) Zoom in of the mineral region showing three spectra of particle RA-QD02-0214 with different mineral compositions. (Color figure can be viewed at wileyonlinelibrary.com.)

olivine (Hamilton [2010] for olivine identification; Omori [1971] for pyroxene identification).

The unequivocal attribution of IR bands to precise minerals, silicates in particular, is difficult in this kind of 3-D measurement due to the restricted range of wavelength accessible with the setup and the relatively low spectral resolution and low signal to noise ratio that are necessary to achieve the whole tomography measurement (180°) in a reasonable amount of time. X-CT is more efficient to determine most of the mineral composition in 3-D, but IR has the main advantage to be able to detect and precisely identify organic components. Here, we observed spatially correlated signatures attributed to the organic glue surrounding the samples. These signatures are present in almost all spectra of the sample (see green spectrum in Fig. 5a). As we measured the signal coming from a projected column, we always measured glue surrounding one side of the particle. The glycol phthalate glue used to fix the samples to the carbon fibers was responsible for the following IR bands: a C-O stretching mode band at 1110 cm^{-1}, a CH_3 deformation mode band at 1373 cm^{-1}, and a CH_3 stretching mode band (symmetrical at 2864 cm^{-1} and asymmetrical at 2962 cm^{-1}), a small band at 3062 cm^{-1} due to CH aromatic stretching, a large OH stretching band between 3000 and 3750 cm^{-1} due to alcohol function. The ester group COO conjugated to the aromatic cycle of phthalate explained the position of the C = O vibration band mode at 1690–1790 cm^{-1} and the C = C vibration band mode at 1604 cm^{-1}. The feature between 2300 and 2400 cm^{-1} was due to CO_2 as the measurement was performed in open air. All these bands were easily detected in the red spectrum of Fig. 5a extracted from an area mainly composed of glue, in a projection of particle RA-QD02-0214.

Finally, for the five particles, we detected a band at 1180 cm^{-1} (see Fig. 5b) in localized spots (5 µm in size). This band was not spatially related to the glue. The peak position of the band suggested a tentative attribution to a sulfate component.

Once the bands are identified, we studied their spatial distribution in the projections. We observed that glue and silicates were spatially separated. The sulfate

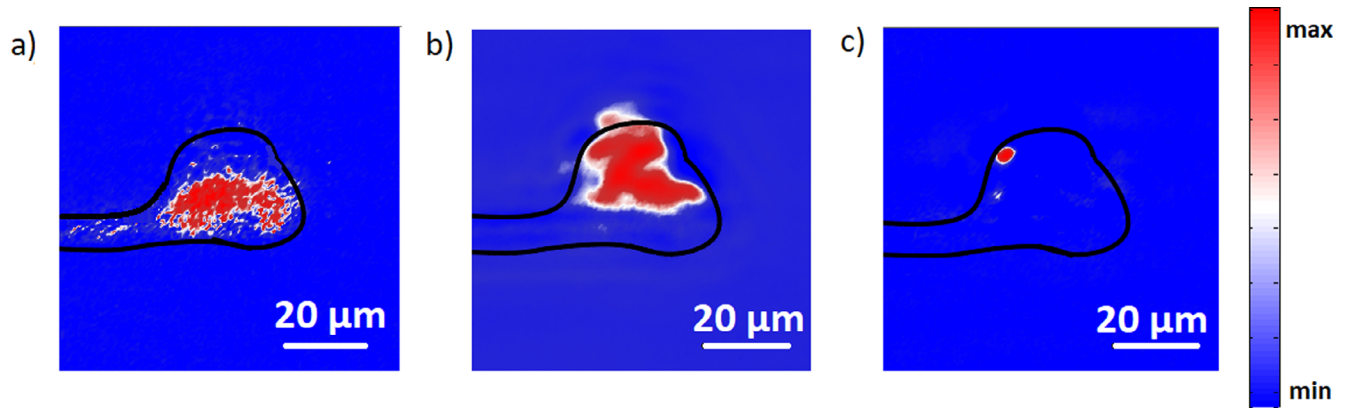

Fig. 6. IR maps showing the spatial distribution of (a) aliphatic CH stretching band of the glue, (b) the left shoulder of the large silicate band, and (c) the sulfate band, for one projection of particle RA-QD02-0214. (Color figure can be viewed at wileyonlinelibrary.com.)

was also well separated from the other components. Figure 6 shows the spatial distribution of these three phases for one projection. The contour of the grain and the needle glued to it, shown in black, is obtained using the projection of the continuum at 2.8 µm.

For the particle RA-QD02-0214, we separated the olivine and the Ca-rich pyroxene by using the intensity of the second derivative at the wavelength corresponding to the maximum of the strongest Si-O band of each mineral in the raw spectra.

In the following, we will present the 3-D structure reconstructed by IR and X-rays for one particle of each kind defined above.

The Case of a Particle Dominated by One Component

In Fig. 7, we see in colors the IR reconstruction of the aliphatic CH bands characteristic of the glue (panel a) and the silicate large band reconstruction (panel b), superimposed to the X-ray outline (gray) of particle RA-QD02-0223. IR- and X-data agreed quite well, considering that these were the raw reconstructed data before applying any filter on IR voxels. All voxels corresponding to the extra-terrestrial sample (according to X-CT) contained the silicate band in IR data. We evaluated a Pearson product-moment spatial correlation coefficient of 0.65 between the reconstruction of silicates obtained by IR and X-ray analyses. This coefficient was obtained with the raw data. When we applied the shape model from X-ray data to the IR data (see the Shape Model Obtained from X-ray Data section), that is, forcing to zero IR voxels outside the sample (according to X-ray data), we obtained a spatial correlation coefficient between the two data sets of 0.90. By doing this, we removed the effects of the IR diffraction and diffusion around the sample.

The mineral compound and the glue surrounding it are well separated. The spatial correlation coefficient between the broad silicate band and the aliphatic CH band was 0.13. Such a low value indicates the absence of correlation between these two phases and proved that IR reconstruction did not introduce any major bias.

We detected a small heterogeneity in the IR spatial distribution of the silicate broad band. We have plotted the variation of the reconstructed intensity at 10 µm along one line in the particle RA-QD02-0223 (see Fig. 8a). We observed a variation of 10% around the average value (see black dashed line in Fig. 8b) inside this sample made of only one component. This oscillation gives an estimation of the uncertainty in the signal amplitude. Diffraction inside the sample varies according to the angle of incidence and induces small variations in the amplitude of the absorbed signal. This phenomenon induces reconstruction artifacts of the same order of magnitude and is responsible for the variation of 10% in the intensity in IR-reconstructed data. This heterogeneity was not as strong in X-CT data, as we measured variations of intensity of only 5% inside the Ca-poor pyroxene. Moreover, diffraction is responsible for the dispersion of the intensity at the edge of the sample. Even if the spatial resolution is limited by the diffraction, oversampling helps us to detect structures beyond the spatial resolution. Studying the magnitude of the deviation from the Heaviside function at the physical edge of the sample, we can estimate a spatial uncertainty of 4 µm at 10 µm on the IR-reconstructed data. We filtered the IR data using the X-ray data (see blue curve for the filtered data), and we obtained a more realistic shape.

The Case of a Particle with Two Components

For polymineralic particles, in addition to the reconstruction mentioned above, we also performed individual IR reconstructions for specific minerals based on the intensity of the second derivative. Figure 9a

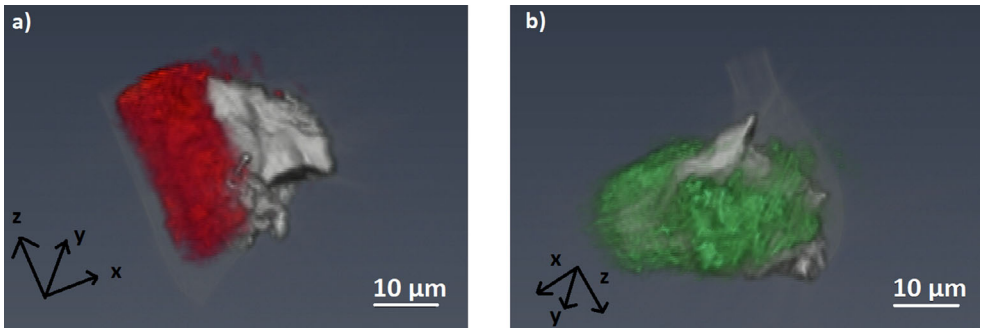

Fig. 7. 3-D IR detection of glue (in red, [a]) and mineral (in green, [b]) for particle RA-QD02-0223. The X-ray data are represented in gray scale (with the glue and the needle in very light gray and the extra-terrestrial mineral in a more intense gray). (Color figure can be viewed at wileyonlinelibrary.com.)

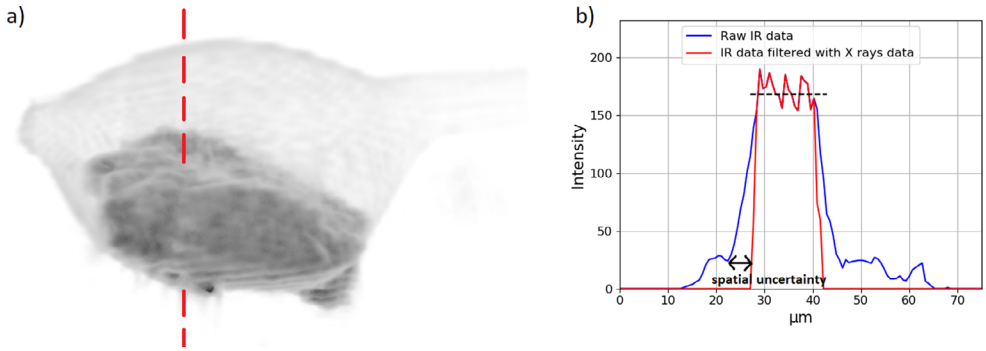

Fig. 8. a) The sample RA-QDO2-0214 with a dashed red line crossing it and (b) the intensity of the reconstructed silicate band along the dashed red line as a function of the position along this line. The blue curve represents the raw IR data, and the red curve is after filtering it using the X-ray data. The black dashed line is the average intensity of the silicate bands. Inside the sample (between 30 and 40 µm), the two lines are superimposed (Color figure can be viewed at wileyonlinelibrary.com.)

shows the X-ray data for the particle RA-QD02-0214. In Fig. 9b, we can see the distribution in the IR reconstruction of olivine and Ca-rich pyroxene. The IR reconstruction based on the second derivative agreed well with the distribution of minerals measured by X-CT. Measurement of the spatial correlation coefficient between IR and X-rays gives, respectively, 0.63 and 0.61 for olivine and pyroxene (with shape model). This coefficient is smaller than the one calculated for the particle RA-QD02-0223 described above, probably because the second derivative spectra are more sensitive to noise.

Another way of representing the microtomography data is to extract slices from the 3-D reconstructed sample. In Fig. 10, we report slices (xy) for z = 14 µm inside the sample. The two mineral phases and the organic phase are represented. Once again, we clearly see the separation between olivine and pyroxene in the slices with both IR microtomography and X-CT. We can notice small organic signatures around the particle; they represent few percent of the maximum value of organic concentration (less than 20%). They are probably due to the detection of the thin layer of resin around the sample, used to protect it from oxidation (Tsuchiyama et al. 2011).

The Case of a Particle with Multiple Components

The more complex particle RA-QD02-0232 is shown in Fig. 11, where we present three different slices (yz) spaced by 2 µm in x from each other. This particle was mainly composed of Ca-poor pyroxene with different smaller inclusions of about 2–5 µm in size. For this particle, the spatial correlation coefficient between the IR and X-rays distributions of the silicate was 0.74 (with shape model). The difference between this coefficient and the one calculated for the particle RA-QD02-0223 was probably due to the presence of minor phases that were detected only in the X-ray data.

The inclusions were clearly detected in the X-CT data as troilite or chromite (bright points) and plagioclase (black spots), but they were barely recognizable in the IR data. Indeed, in the IR data, the silicate bands decrease by 25% where troilite or chromite is detected with X-CT. The range of variation is two times bigger than the one due to reconstruction artifacts visible on the particle dominated by one

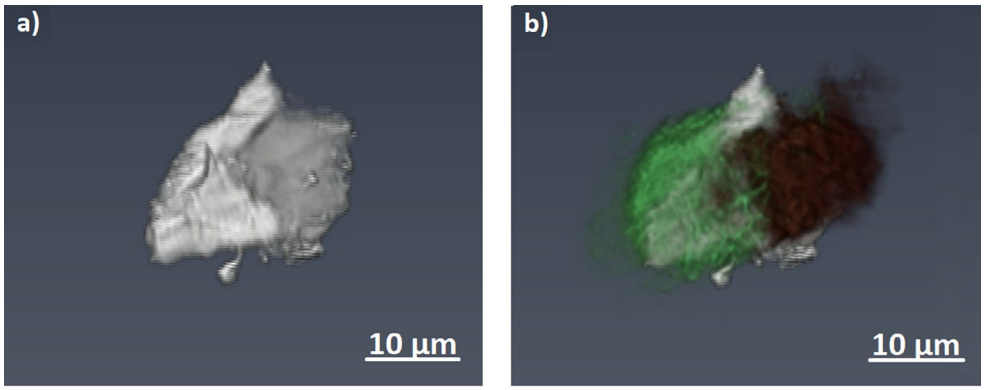

Fig. 9. Detection and separation of olivine and pyroxene minerals in 3-D for RA-QD02-0214. a) X-ray data where only the particle (and not the glue) is represented and the two levels of grays, proportional to the different LAC at 8 keV, show the olivine (light gray) and the Ca-rich pyroxene (dark gray). b) IR data superimposed onto X-ray data, with IR reconstruction of olivine in green and Ca-rich pyroxene in brown (Color figure can be viewed at wileyonlinelibrary.com.)

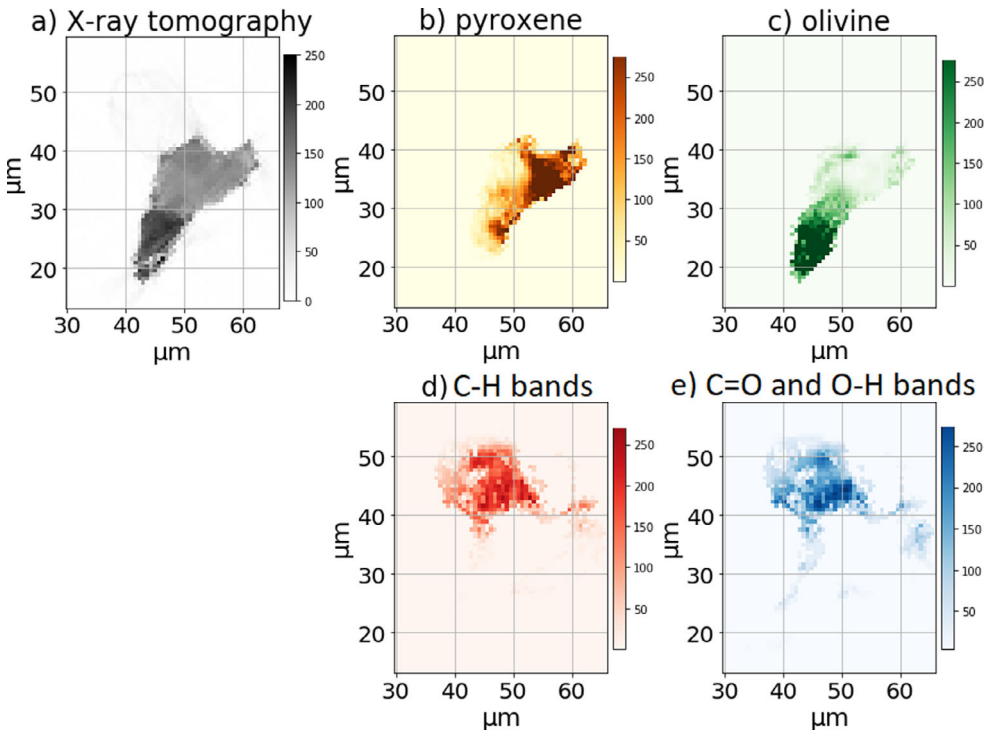

Fig. 10. Slices (xy) extracted from the reconstruction of particle RA-QD02-0214 (a) X-ray LAC data, (b) IR pyroxene band, (c) IR olivine band, (d) IR C-H band, and (e) IR C = O aliphatic band (Color figure can be viewed at wileyonlinelibrary.com.)

component. This implies that, for small mineral inclusions, even if we cannot identify them precisely because of the low signal to noise ratio in our data, we can at least predict their presence and their position.

Paris Meteorite Particle

The last analyzed sample was a particle from the Paris meteorite matrix. The Paris particle showed heterogeneity at a smaller scale than Itokawa's particles. Using IR data, we observed an intimate mixture of organic and mineral meteoritic phases. The main IR band observed in the spectra of the Paris sample was the silicate Si-O band around 1000 cm^{-1}. We observed a broad band with several small subfeatures, essentially due to pyroxenes, olivine, amorphous, and hydrated silicates (Dionnet et al. 2018a). A carbonate spectral contribution was also present around 1460 cm^{-1} in some well-localized spots of the sample (see Fig. 12c). Water bending and stretching modes around 1633 cm^{-1}

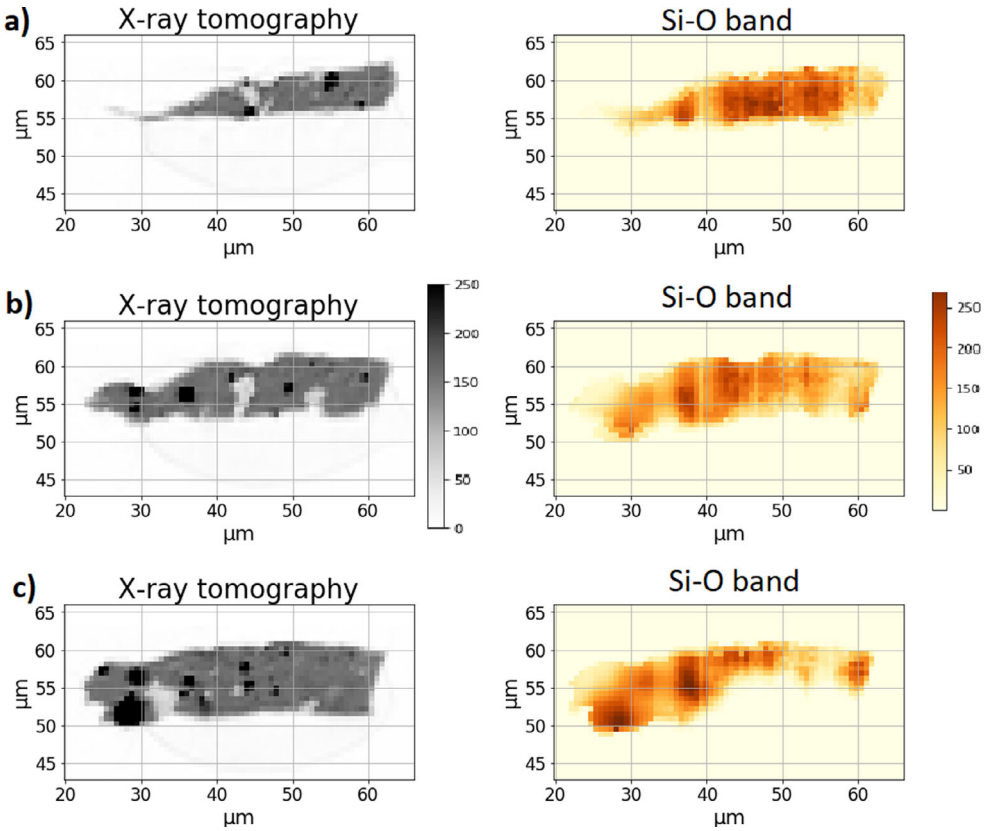

Fig. 11. Polymineralic particle RA-QD02-0232 reconstruction from X-ray LAC data (left), and from the IR silicate band (right) for (a) slice (yz) x = 3.3 µm inside sample, (b) slice (yz) x = 5.3 µm, and (c) slice (yz) x = 7.3 µm (Color figure can be viewed at wileyonlinelibrary.com.)

and 3000–3700 cm^{-1} were very strong (see Fig. 12c). Some spectra also exhibit a weak band at about 3660–3670 cm^{-1} due to structural hydroxyl (–OH) stretching mode (Dionnet et al. 2018a).

Organic signatures were also detected in the spectra of Paris. Aromatic carbons were responsible for the aromatic C-H stretching at 3045 cm^{-1}, and aromatic C = C modes at about 1600, 1510, and 1250 cm^{-1}. A carbonyl (C = O) band is visible around 1730. Aliphatic CH_2 and CH_3 groups were identified using the stretching modes between 2854 and 2958 cm^{-1} and to the bending and deformation modes in the region 1300–1400 cm^{-1}. The identification of organic components is based on the papers of Matrajt et al. (2004), Dartois et al. (2005), Merouane et al. (2012), Yesiltas and Kebukawa (2016), and Dionnet et al. (2018a).

X-ray microtomography was used to characterize the physical properties of the components identified by IR to better understand their assembly. For this particle, we estimated a porosity of 4.6% ± 1% present both as fractures and as circular vesicles. The X-CT data presented a heterogeneity of the mineral phases at the submicron scale, showing the complexity of the assembly of the different components of the mineral phase (see Fig. 12b).

After the application of the shape model provided by the X-ray data, we finally obtained the 3-D spatial distribution of the broad band of the silicates, the carbonates, the water, and the aliphatic CH. Figure 12 shows a slice of the 3-D distribution of the aliphatic organic matter. For the first time, we were able to estimate the number of aliphatic CH oscillators for each voxel. We found an average number of 2×10^{20} oscillators cm^{-3}. We studied the spatial distribution of the CH abundance and we found that, in some selected areas, the aliphatic CH abundance was about three times richer than the average value. A video with the reconstructed distribution of OH, CH, and carbonates is available as supporting information.

DISCUSSION

Composition of the Five Itokawa Samples

For the five particles, IR spectra confirmed the X-CT detection concerning the major phases (see Table 2). However, it is interesting to see how the plagioclase

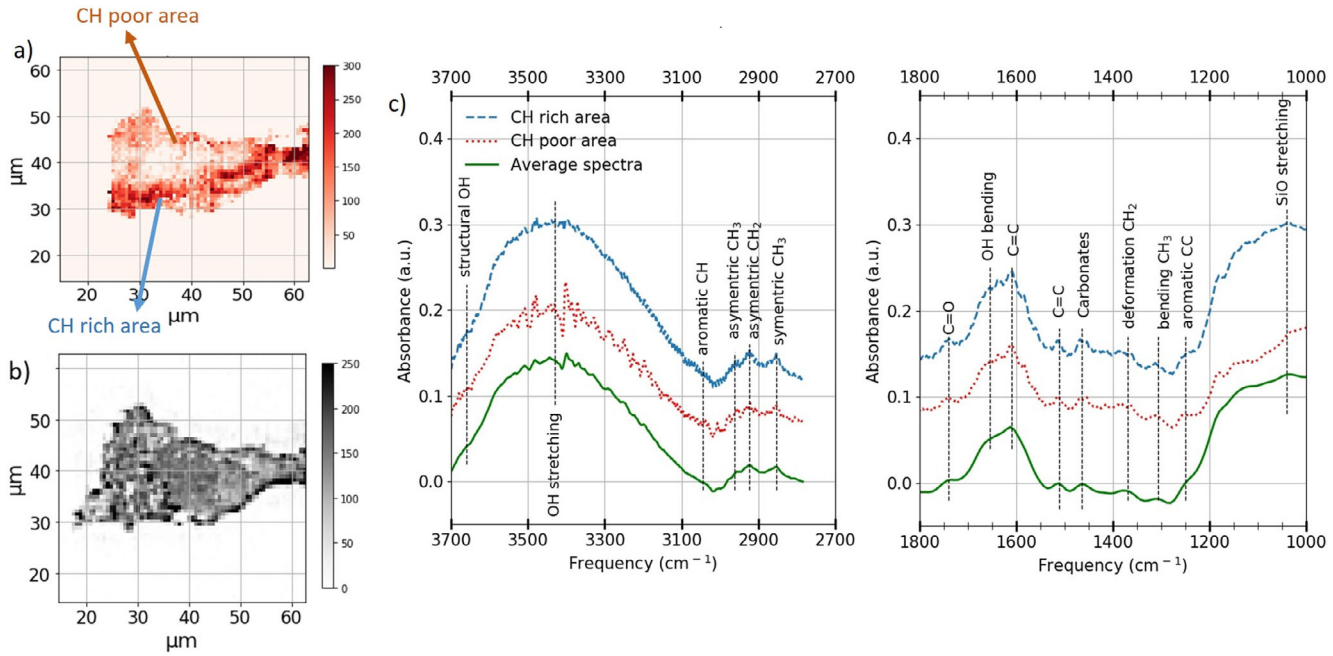

Fig. 12. a and b) Slices extracted from the reconstruction of the Paris meteorite fragment for CH aliphatic (a) and X-ray LAC data (b). c) Spectra of the Paris meteorite fragment obtained from the high resolution acquisition measurement before reconstruction, the average spectra are shown in green, a spectrum of a pixel rich in aliphatic organics in blue, and a spectrum with a low abundance of aliphatic organics in green. (Color figure can be viewed at wileyonlinelibrary.com.)

component was not detected by IR contrary to the sulfate (see Fig. 6c). With the X-CT, we observe plagioclase, present as small inclusions in our particles (about 5 µm), but we cannot detect them with FT-IR microtomography due to a bad spectral contrast between plagioclase Si-O bands and other major silicate Si-O bands and we were not able to differentiate it from the main silicate contribution. Collecting spectra with a higher spectral resolution could help to detect them in the projections. In our current setup, this would increase significantly the duration of the IR tomography measurements. The use of the brighter synchrotron source instead of the globar source would enhance the signal to noise ratio with a reduced number of scans.

Chromite, troilite, and taenite are additional components detected by X-ray analyses, but they are not detectable by IR spectroscopy in the range investigated here. Chromite has IR bands at 480 and 650 cm^{-1} (Lane et al. 2002) and much weaker bands at around 800 and 1000 cm^{-1} (Cloutis et al. 2004); troilite at 232, 263, 303, and 434 cm^{-1} (Hony et al. 2002); and taenite has no IR-active vibrational modes (Murata et al. 2007). Their presence is common in chondrites (Fehr and Carion 2004). The majority of these bands are not detectable by our setup, except the one around 1000 cm^{-1}, but as it is close to the large silicate band, it is not possible for us to distinguish chromite inside our samples using IR.

Itokawa particles are known to be compatible with an LL-chondrite-like composition. For instance, the study of oxygen isotopic composition of pyroxene, olivine, and plagioclase performed by Yurimoto et al. (2011) and Nakashima et al. (2013) confirmed the link between the Itokawa samples and the LL chondrites. Based on the position of the olivine bands, we identified olivine present in our samples as $Fo_{65\pm5}$. The Fo or En contents (in atom%) based on the X-CT (dual-energy tomography) are measured and we obtained Fo_{70} for RA-QD02-0214, En_{73} for RA-QD02-0223, En_{74} for RA-QD02-0232, Fo_{68} for RA-QD02-0156, and Fo_{67} for RB-QD04-0046. Unfortunately, the spectral resolution was not good enough to detect such variations with IR. Our measurements are consistent with the ones previously performed on other Itokawa particles (Nakamura et al. 2011; Bonal et al. 2015) and confirm the link between Itokawa and LL chondrites (typical Fo_{68-74} olivines are detected in LL chondrites according to Kallemeyn et al. 1989).

Most Itokawa particles (between 30 and 180 µm) show an almost homogeneous chemical composition (Nakamura et al. 2011; Tsuchiyama et al. 2011), which indicates that these samples have been thermally annealed. Moreover, complementary studies have shown that most of Itokawa particles are similar to LL5-6 (Abe et al. 2006; Fujiwara et al. 2006). The maximum temperature undergone by minerals containing both Ca-poor and Ca-rich pyroxene is about 800 degrees

Table 2. Comparison between the components detected by IR tomography and dual-energy X-CT.

	Detected components				
Method	RA-QD02-0214	RA-QD02-0223	RA-QD02-0232	RA-QD02-0156	RB-QD04-0046
IR tomography	Ca-rich pyroxene Olivine Sulfate	Ca-poor pyroxene Sulfate	Ca-poor pyroxene Sulfate	Olivine Sulfate	Olivine Sulfate
Dual-energy X-CT	Ca-rich pyroxene Olivine Plagioclase	Ca-poor pyroxene Plagioclase Ca-rich pyroxene	Ca-poor pyroxene Plagioclase Ca-rich pyroxene Chromite Troilite Taenite	Olivine	Olivine Plagioclase Troilite

(Nakamura et al. 2011). Some of the Itokawa particles, about 10%, have undergone lower thermal alteration and are more similar to LL4 (Nakamura et al. 2011; Tsuchiyama et al. 2011).

The sulfates detected in our IR data were localized at the edge of samples (see for instance Fig. 6c), and were not detected by X-CT. Previous works on other Itokawa samples (e.g., Noguchi et al. 2014) did not report the detection of sulfates. Gounelle and Zolensky (2001) discussed the terrestrial origin of sulfates in meteorites. Based on this evidence, we consider that the grains of sulfates detected in our particles may be due to a terrestrial alteration (reaction with atmospheric water) occurred between the X-CT and the IR measurements.

Using FT-IR microtomography, we also studied the composition of the contaminant organic matter (glue in this case). Molecular functions such as C-O, O-H, C-H, and C = C were easily detected. These functions are commonly observed in other extra-terrestrial materials (primitive meteorites and dust) and are an excellent proxy of the composition of organic materials (Merouane et al. 2012). This is a promising result for future studies to be conducted on samples containing extra-terrestrial organic matter. In particular, we consider infrared 3-D microtomography an excellent starting point in a multi-analytical sequence to be applied on samples returned from asteroids and comets as it will provide a first quick look at the composition and 3-D distribution of carbonaceous materials. In the case of carbon-rich extra-terrestrial materials, a preparation with minimal contamination by terrestrial organics should be envisaged. Welding the sample to a needle by means of focused ion beam preparations is currently being studied (Dionnet et al. 2018b).

Study of the Organic Component of the Paris Meteorite

As described in the Results section, we have detected the organic signatures in the IR data set of the Paris meteorite. The preparation and welding in the FIB microscope imply the cracking of an organo-metallic gas and it could have induced a small contamination by organic matter on the area of welding, so our first concern was to check the meteoritical nature of the organic matter detected by FT-IR microtomography. We carefully checked the welding area by FT-IR spectroscopy and we did not notice any peculiar IR signature of organics different from the rest of the sample, nor a higher quantity of organics near the welding area. Moreover, we performed some additional measurements with a Raman microspectrometer and, when looking for organic contamination at the transition between the needle and the sample, we observed a very weak and localized (<3 μm) signature of polyaromatic carbons (D and G bands) with a different spectral profile with respect to the typical D and G bands observed in the rest of the Paris meteorite (see, e.g., the Raman spectra of Paris reported by Dionnet et al. 2018a). In particular, the contaminated area showed much broader D and G bands that are characteristic of a highly disordered (hydrogen-poor) amorphous carbon. Thus, we were able to distinguish the indigenous organics of our Paris sample, observed by FT-IR microtomography, from a weak and localized amorphous carbon contamination, visible only with Raman microspectrometry.

Moreover, studying the aliphatic organics detected by FT-IR, we compared the number of CH oscillators per cm^{-3} of the sample to the one, normalized to the thickness, to a previously measured, crushed sample of Paris (Dionnet et al. 2018a), and we found a similar value. At the scale of whole fragments, the average number of oscillators per cm^{-3} obtained for the sample studied in 3-D in this paper differs by 17% from the one obtained in the sample published in Dionnet et al. (2018a) on a crushed sample. As described below, the quantity of CH oscillators can vary inside a single grain of Paris meteorite by a factor of three; thus, a sample by sample variation of 17% is insignificant.

In this sample, we emphasized many small bands characteristic of the organic moieties. All the bands observed in previous studies of the IOM of carbonaceous chondrites led by Kebukawa et al. (2011) and Orthous-Daunay et al. (2013) were also present in our sample and the structure of the bands (shape and relative intensity) is similar to the one described by Orthous-Daunay et al. (2013). Based on the IR spectrum, the organics of Paris resemble those of other CM2 (Bells and Murchison) and CR2 (EET92042) measured by Kebukawa et al. (2011). Kebukawa et al. (2011) and Orthous-Daunay et al. (2013) reported spectra of IOM once it is extracted from the original meteorites. Here, we show the ability of FT-IR microtomography to detect small organic features without any chemical (e.g., extraction) or physical (e.g., crushing) destructive processes. This makes FT-IR microtomography particularly worthwhile as a preliminary analysis to characterize samples rich in organic matter before more invasive techniques.

Concerning the spatial heterogeneity of the aliphatic matter, we put particular emphasis on the detection of a zone rich in organics that appears in the lower left area of the fragment (see Fig. 12a): this structure is 5 μm large and 2 μm long and it shows an abundance of aliphatics about three times higher than the average of the whole fragment. This zone is also rich in water (abundance of water at least two times higher than the average). The 3-D correlation (voxel by voxel) between the distribution of water and aliphatic CH is 0.81, which indicates a strong spatial link between these two phases. We also observe a strong 3-D correlation between water and silicates (0.84). These co-localizations suggest that aliphatic matter formation could be promoted by or related to the presence of hydrated silicates. This is consistent with the results obtained on another fragment of Paris (Dionnet et al. 2018a) and with the ones established by Yesiltas et al. (2016).

3-D Structure and Porosity

As all the formation/alteration processes for solid materials in space occur in 3-D, we should be able to observe evidence of parent body processes in 3-D studies of extra-terrestrial samples (Ebel and Rivers 2007). Moreover, using the 3-D view, we can remove ambiguities due to overlapping pixels in 2-D. Finally, by combining X-CT to FT-IR microtomography, we can investigate chemical and physical information in 3-D: X-CT gives information on the shape and on the porosity, while FTIR microtomography gives information about the abundance of the organics and the hydration state. Here, we present some information obtained with X-CT about the physical structuration of our samples.

We were able to evaluate the porosity for our five Itokawa particles by counting the number of empty voxels divided by the number of voxels containing samples (see Tsuchiyama et al. [2011] for technical details). We obtained porosity of: 1.9% for RA-QD02-0156, 5.5% for RA-QD02-0214, 7.7% for RA-QD02-0223, 4.2% for RA-QD02-0232, and 10.1% for RB-QD04-0046, with an error estimated at 1% (based on the values obtained by considering a variable threshold for the detection of the pores within the range of LAC noise in empty areas). These values are in good agreement with the average porosity of LL chondrites (8.2 ± 5.5%) according to Consolmagno et al. (2008), which compiled measurements performed with different methods (point-counting void spaces visible in SEM backscatter images, gas pycnometry methods, etc.). The main contribution to the porosity was located into microcracks (about 1 μm thick, see red arrow in Figs. 4b and 4c) and we did not observe spherical pores. This structuring is similar to that of ordinary chondrites. Microcracks are produced by passage of shock waves caused by impact cratering on the parent bodies (Consolmagno et al. 2008). This confirms that impacts played an important role in the evolution of Itokawa (Nakamura et al. 2012).

Using the X-CT study of the Paris sample, we derived its shape, which helps to filter artifacts in the FT-IR reconstruction and we noted the complexity of the mineral assembly, observing variations of the mineral composition at the submicron scale. We estimated a porosity of 4.6% ± 1%. This value is lower than the one expected for a CM (23.1% ± 4.7%) determined by Consolmagno et al. (2008). The difference can be explained by the fact that we studied a single grain, and that a part of the macroporosity (pores bigger than the few micrometers) was not measured in this paper. Indeed, the presence of such big vesicles inside our sample would have made it too fragile, and the grains would have divided into smaller individual particles. Another limitation is our incapability to detect vesicles smaller than the pixel size (0.13 μm). Thus, the different porosity values in micrometric single grains and macroscopic samples suggest that the majority of the porosity is located in pores bigger than few micrometers or smaller than the pixel size (0.13 μm) for the CM Paris.

Advantages and Limitations of FT-IR Microtomography

For future analysis of extra-terrestrial materials collected by sample return missions, it will be necessary to establish an optimized multi-analytical sequence able

to maximize the scientific output at every step. Especially, the study of organic matter will be a critical point. It is thus important to understand the potential contribution of FT-IR microtomography, to highlight its complementary role with respect to X-CT, and to recognize its limits. Being totally nondestructive, FTIR microtomography and its characterization of the organics could be the first step of analyses. Some studies suggested that X-CT can cause some damage to the organics (see e.g., Sears et al. 2016; Hanna and Ketcham 2017); however, this strongly depends on the experimental conditions used (namely energy and photon density). In any case, in future studies, it will be important to perform FTIR microtomography before X-CT to be able to address this issue.

In this study, particle RA-QD-0223 gave us the opportunity to reconstruct in 3-D both organic and mineral components from the IR data and to delineate them accurately. The study of particle RA-QD-0214 provided an example of good 3-D separation of mineral phases by IR spectroscopy, and finally, the more complex particle RA-QD02-0232 provided an opportunity to investigate to which extent IR microtomography was sensitive to the mineral heterogeneity.

The intrinsic lower spatial resolution of IR with respect to X-rays represents the most obvious limit of IR microtomography. This can be seen by comparing particles RA-DQ02-0214 and RA-QD02-0232: in the former, olivine and pyroxene were well detected and separated, with each one of them sizing about 1000 μm^3; in the latter, the small (about 30 μm^3) pyroxene inclusions were hardly detected by IR. Although our IR measurements are diffraction limited, it is still possible to detect grains that are smaller than the wavelength, as it can be seen in Fig. 6, where a 4 μm-sized sulfate grain was detected on the surface of particle RA-QD02-0214 using a wavelength of about 8.5 μm. In this respect, it is much harder to distinguish two phases with quite close spectra (e.g., Ca-rich pyroxene and Ca-poor pyroxene) than two phases with high spectral contrast (e.g., sulfates and silicates, see also Sandt et al. 2019). This explains why we are able to detect small grains of sulfates inside our samples but not grains of plagioclase. The detection of minor phases with small absorption bands might be improved by increasing both the spectral resolution and the signal to noise ratio in the IR spectra. This will be achieved in the next future by coupling the tomography setup with the IR synchrotron beam. In principle, the detection of small phases and/or phases with no active IR vibrations in the chosen range may also be also achieved indirectly thanks to the detection of empty spaces in the 3-D reconstructed data. We explored this possibility in particle RA-QD02-0232 and we found that diffraction and diffusion hinder such detection if the phases are smaller than 30 μm^3. Even if we detected a local decrease of intensity in the silicate band, there remained a range of variations from reconstruction biases due to relatively low spectral signal to noise ratio and diffraction/diffusion effects.

Even if the IR has the disadvantage of lower spatial resolution than the one of the X-rays, it remains a powerful tool to detect and analyze organic materials. Materials composed of light elements, such as organics and water, can be seen by using phase contrast in X-ray CT. We can obtain phase and absorption contrasts simultaneously by SIXM, a kind of X-ray CT (Takeuchi et al. 2013), and this method was applied to extraterrestrial materials (e.g., Tsuchiyama et al. 2016). However, we cannot specify a type of organics and cannot discriminate water from organics by this method. So, the combination of X-ray phase CT and IR is a very useful and promising method for 3-D observation and analysis of organics and water. Indeed in this study, we detected and reconstructed bands of molecular functions such as the aliphatic and aromatic organics, C-O, and O-H stretching due to hydration inside a primitive meteorite. We detected heterogeneity in meteoritical organic matter distribution and in the distribution of water. Combined with the X-ray data which give mineral identification, we can then discuss the degree of hydration of minerals or the presence of organics. Two voxels with the same LAC can correspond to areas with very different levels of hydration and with a different abundance of organic matter, and thus with very different histories. FT-IR data can then remove ambiguities present in the X-ray data. For example, in our data sets, we have noticed the presence of voxels with the same LAC (22.5 $cm^{-1} \pm 0.1$ cm^{-1} at 17.6 keV), thus similar from the point of view of the X-ray measurement, but with very different abundance of organic matter observed by FT-IR microtomography (from voxels with a very low concentration in organics matter to voxels with a concentration in organic two times higher than the average value). At the opposite, the detection of substructure at a small scale using X-rays brings information on the agglomeration processes, the structuration of the matter or strength of secondary processes (via the study of the shape of the vesicles), not detectable with FTIR, but useful to interpret how the sample has evolved since the formation of its parent body.

The X-ray and IR data sets proved to be quite complementary, as the former provided structural information such as shape, porosity, density, and distribution of mineral phases at very good resolution

(see Tsuchiyama et al. 2011), while the latter not only provided molecular information about minerals but also provided significant molecular information about organics and hydration. Each of them is able to remove some ambiguity concerning the information obtained with the other technique: as we have shown, X-CT brings complementary information regarding the structure and the shape model, and IR-CT can discriminate voxels with the same X-ray signal but with different abundance of water and organics.

Our results are highly encouraging for the detection of organics in particles collected by the next generation of sample return missions from possibly carbon-rich small asteroids. In particular, it will be crucial to be able to trace the 3-D distribution of organics and water in Hayabusa2 and OSIRIS-REx samples. FTIR microtomography combined with X-CT on these samples will probably provide key information about the formation and evolution of organic matter in primitive bodies and its relation with the mineral phases, as we will be able to study 3-D spatial relation between these different phases.

Finally, some disadvantages of IR, such as scattering and diffraction at the particle edges, can be compensated by combining with X-CT. Indeed, these processes introduce a blurring of the 3-D reconstructed IR images, but X-ray data provide an excellent shape model to improve the IR reconstruction, and thanks to this study, we stress the importance of combining IR data to X-ray data.

CONCLUSIONS

The implementation of a 3-D IR setup (similar to the one described by Martin et al. 2013) and for the first time the combination of IR microtomography with X-ray microtomography are the two major technical issues of this work. This setup is now available for the analysis of different extra-terrestrial materials and in particular for future samples returned from space. It will soon be improved by combining the FPA detector with the synchrotron IR beam.

In this paper, we have reported a combined IR and X-ray microtomography analysis on Itokawa particles brought back to Earth by Hayabusa and on a fragment from a primitive carbonaceous chondrite. These samples were a great opportunity to implement such combined analytical approach and to explore the limitations of the IR analysis. FT-IR microtomography is a promising tool to be applied on extraterrestrial materials, thanks to its noninvasive sensitivity to both minerals and organics. When compared with other X-ray-based spectroscopic techniques, the main limiting factor of FT-IR microtomography remains its intrinsic low spatial resolution due to the long wavelength. It is then interesting to combine it with techniques with stronger spatial resolutions. Moreover, the characterization of the organic phases by FT-IR microtomography will be a critical point for future samples, and we have shown that IR-CT can be completed by X-CT to balance its limitations and to help characterize the 3-D context of the detected organics.

We have recently shown that nondestructive FT-IR microtomography can be performed on samples without invasive sample preparations using a focused ion beam (Dionnet et al. 2018b). With this preparation, the contamination by terrestrial organics is minimal and localized, which makes it a promising preparation protocol for tomography of organic-rich extra-terrestrial materials. Moreover, it will be possible to recover the samples after the analysis. In a sequence of analysis, micro-FT-IR 3-D spectral imaging combined with X-ray microtomography can thus provide a first characterization of whole particles, to identify areas of interest, to spatially separate organics and minerals, and thus to provide useful information before subsequent destructive analysis. This will be particularly useful in the near future, with the return of precious carbon-rich extraterrestrial materials thanks to sample return missions.

Acknowledgments—This work is supported by the "IDI 2015" project funded by the IDEX Paris-Saclay (Grant ANR-11-IDEX- 0003-02). The FT-IR microspectroscopy activities are supported by grants from Région Ile-de-France (DIM-ACAV) and SOLEIL. This work has been funded by the Centre National d'Etudes Spatiales (CNES-France, Hayabusa2 mission) and by the ANR project CLASSY (Grant ANR-17-CE31-0004-02) of the French Agence Nationale de la Recherche. This work was partly supported by the French RENATECH network. We wish to thank the Italian Space Agency (ASI, Italy) contract no. I/024/12/2 and MIUR, contracts PNRA16-00029 and PRIN2015-20158W4JZ7. We are grateful to the JAXA Curator for allocating the Hayabusa particles. We thank T. Yada and L. Bonal for useful discussion, B. Zanda for providing the Paris meteorite sample, and the ANATOMIX team (SOLEIL) for their help with Avizo. We thank the two reviewers for their useful comments and suggestions.

Editorial Handling—Dr. Donald Brownlee

REFERENCES

Abe M., Takagi Y., Kitazato K., Abe S., Hiroi T., Vilas F., Clark B. E., Abell P. A., Lederer S. M., Jarvis K. S., Nimura T., Ueda Y., and Fujiwara A. 2006. Near-infrared

spectral results of asteroid Itokawa from the Hayabusa Spacecraft. *Science* 312:1334.

Alexander C. M. O'D., Fogel M., Yabuta H., and Cody G. D. 2007. The origin and evolution of chondrites recorded in the elemental and isotopic compositions of their macromolecular organic matter. *Geochimica et Cosmochimica Acta* 71:4380–4403.

Beck P., Garenne A., Quirico E., Bonal L., Montes-Hernandez G., Moynier F., and Schmitt B. 2014. Transmission infrared spectra (2–25 lm) of carbonaceous chondrites (CI, CM, CV–CK, CR, C2 ungrouped): Mineralogy, water, and asteroidal processes. *Icarus* 229:263.

Bonal L., Brunetto R., Beck P., Dartois E., Dionnet Z., Djouadi Z., Duprat J., Füri E., Kakazu Y., Montagnac G., Oudayer P., Quirico E., and Engrand C. 2015. Visible-IR and Raman microspectroscopic investigation of three Itokawa particles collected by Hayabusa: Mineralogy and degree of space weathering based on nondestructive analyses. *Meteoritics & Planetary Science* 50:1562–1576.

Bradley J. P., Humecki H. J., and Germani M. S. 1992. Combined infrared and analytical electron microscope studies of interplanetary dust particles. *The Astrophysical Journal* 394:643–651.

Brownlee D., Tsou P., Aleon J., Alexander C. M. O. D, Araki T., Bajt S., Baratta G. A., Bastien R., Bland P., Bleuet P., Borg J., Bradley J. P., Brearley A., Brenker F., Brennan S., Bridges J. C., Browning N. D., Brucato J. R., Bullock E., Burchell M. J., Busemann H., Butterworth A., Chaussidon M., Cheuvront A., Chi M., Cintala M. J., Clark B. C., Clemett S. J., Cody G., Colangeli L., Cooper G., Cordier P., Daghlian C., Dai Z., D'Hendecourt L., Djouadi Z., Dominguez G., Duxbury T., Dworkin J. P., Ebel D. S., Economou T. E., Fakra S., Fairey S. A. J., Fallon S., Ferrini G., Ferroir T., Fleckenstein H., Floss C., Flynn G., Franchi I. A., Fries M., Gainsforth Z., Gallien J.-P., Genge M., Gilles M. K., Gillet P., Gilmour J., Glavin D. P., Gounelle M., Grady M. M., Graham G. A., Grant P. G., Green S. F., Grossemy F., Grossman L., Grossman J. N., Guan Y., Hagiya K., Harvey R., Heck P., Herzog G. F., Hoppe P., Horz F., Huth J., Hutcheon I. D., Ignatyev K., Ishii H., Ito M., Jacob D., Jacobsen C., Jacobsen S., Jones S., Joswiak D., Jurewicz A., Kearsley A. T., Keller L. P., Khodja H., Kilcoyne Al D., Kissel J., Krot A., Langenhorst F., Lanzirotti A., Le L., Leshin L. A., Leitner J., Lemelle L., Leroux H., Liu M.-C., Luening K., Lyon I., MacPherson G., Marcus M. A., Marhas K., Marty B., Matrajt G., McKeegan K., Meibom A., Mennella V., Messenger K., Messenger S., Mikouchi T., Mostefaoui S., Nakamura T., Nakano T., Newville M., Nittler L. r, Ohnishi I., Ohsumi K., Okudaira K., Papanastassiou D. A., Palma R., Palumbo M. E., Pepin R. O., Perkins D., Perronnet M., Pianetta P., Rao W., Rietmeijer F. J. M., Robert F., Rost D., Rotundi A., Ryan R., Sandford S. A., Schwandt C. S., See T. H., Schlutter D., Sheffield-Parker J., Simionovici A., Simon S., Sitnitsky I., Snead C. J., Spencer M. K., Stadermann F. J., Steele A., Stephan T., Stroud R., Susini J., Sutton S. R., Suzuki Y., Taheri M., Taylor S., Teslich N., Tomeoka K., Tomioka N., Toppani A., Trigo-Rodriguez J. M., Troadec D., Tsuchiyama A., Tuzzolino A. J., Tyliszczak T., Uesugi K., Velbel M., Vellenga J., Vicenzi E., Vincze L., Warren J., Weber I., Weisberg M., Westphal A. J., Wirick S., Wooden D., Wopenka B., Wozniakiewicz P., Wright I., Yabuta H., Yano H., Young E. D., Zare R. N., Zega T., Ziegler K., Zimmerman L., Zinner E., and Zolensky M. 2006. Comet 81P/Wild 2 under a microscope. *Science* 314:1711–1716.

Brunetto R., Borg J., Dartois E., Rietmeijerc F. J. M., Grossemya F., Sandtd C., Le Sergeant d'Hendecourta L., Rotundib A., Dumasd P., Djouadia Z., and Jammed F. 2011. Mid-IR, Far-IR, Raman micro-spectroscopy, and FESEM–EDX study of IDP L2021C5: Clues to its origin. *Icarus* 212:896.

Campagnola S., Yam Chit H., Tsuda Y., Ogawa N., and Kawakatsu Y. 2018. Mission analysis for the Martian Moons Explorer (MMX) mission. *Acta Astronautica* 146:409–417.

Cloutis E. A., Sunshine J. M., and Morris R. V. 2004. Spectral reflectance-compositional properties of spinels and chromites: Implications for planetary remote sensing and geothermometry. *Meteoritics & Planetary Science* 39:545–565.

Cody G. D., Ade H., Alexander M. O'. D., Araki T., Butterworth A., Fleckenstein H., Flynn G., Gilles M. K., Jacobsen C., Kilcoyne A. l. D., Messenger K., Sandford S. A., Tyliszczak T., Westphal A. J., Wirick S., and Yabuta H. 2008. Quantitative organic and light-element analysis of comet 81P/Wild 2 particles using C-, N-, and O-μ-XANES. *Meteoritics & Planetary Science* 43:353–365.

Consolmagno G. J., Britt D. T., and Macke R. J. 2008. The significance of meteorite density and porosity. *Chemie der Erde* 68:1–29.

Dartois E., Munoz Caro G. M., Deboffle D., Montagnac G., and d'Hendecourt L. 2005. Ultraviolet photoproduction of ISM dust. *Astronomy & Astrophysics* 432:895.

Dionnet Z., Aleon-Toppani A., Baklouti D., Borondics F., Brisset F., Djouadi Z., Sandt C., and Brunetto R. 2018a. Organic and mineralogic heterogeneity of the Paris meteorite followed by FTIR hyperspectral imaging. *Meteoritic & Planetary Science* 53:2608–2623.

Dionnet Z., Aléon-Toppani A., Borondics F., Brunetto R., Buellet A. C., Djouadi Z., King A., Rubino S., and Troadec D. 2018b. FTIR micro-tomography of Five Itokawa particles and one primitive carbonaceous chondrite. *Microscopy and Microanalysis* 24:2100–2101.

Ebel D. S. and Rivers M. L. 2007. Meteorite 3-D synchrotron microtomography: Methods and applications. *Meteoritics & Planetary Science* 42:1627–1646.

Fehr K. L. and Carion A. 2004. Unusual large chromite crystals in the Saint Aubin iron meteorite. *Meteoritics & Planetary Science Suppl* 39:A139–A141.

Flynn G. F., Nittler L. R., and Engrand C. 2016. Composition of cosmic dust: Sources and implications for the early solar system. *Elements* 12:177–183.

Fujiwara A., Kawaguchi J., Yeomans D. K., Abe M., Mukai T., Okada T., Saito J., Yano H., Yoshikawa M., Scheeres D. J., Barnouin-Jha O., Cheng A. F., Demura H., Gaskell R. W., Hirata N., Ikeda H., Kominato T., Miyamoto H., Nakamura A. M., Nakamura R., Sasaki S., and Uesugi K. 2006. The rubble-pile asteroid Itokawa as observed by Hayabusa. *Science* 312:1330–1334.

Gounelle M. and Zolensky M. E. 2001. A terrestrial origin for sulfate veins in CI chondrites. *Meteoritics & Planetary Science* 36:1321.

Hamilton V. E. 2010. Thermal infrared (vibrational) spectroscopy of Mg–Fe olivines: A review and applications

to determining the composition of planetary surfaces. *Chemie der Erde—Geochemistry* 70:7.

Hanna R. D. and Ketcham R. A. 2017. X-ray computed tomography of planetary materials: A primer and review of recent studies. *Chemie der Erde* 77:547–572.

Hewins R. H., Bourot-Denise M., Zanda B., Leroux H., Barrat J. A., Humayun M., Göpel C., Greenwood R. C., Franchi I. A., Pont S., Lorand J. P., Courne C., Gattacceca J., Rochette J. P., Kuga M., Marrocchi Y., and Marty B. 2014. The Paris meteorite, the least altered CM chondrite so far. *Geochimica et Cosmochimica Acta* 124:190–222.

Hony S., Bouwman J., Keller L. P., and Waters L. B. F. M. 2002. The detection of iron sulfides in planetary nebulae. *Astronomy & Astrophysics* 393:L103–L106.

Hoppe P. 2006. NanoSIMS: A new tool in cosmochemistry. *Applied Surface Science* 252:7102–7106.

Kallemeyn G. W., Rubin A. E., Wang D., and Wasson J. T. 1989. Ordinary chondrites—Bulk compositions, classification, lithophile element fractionations, and composition-petrographic type relationships. *Geochimica et Cosmochimica Acta* 53:2747–2767.

Kebukawa Y., Alexander C. M. O'D., and Cody G. D. 2011. Compositional diversity in insoluble organic matter in type 1, 2 and 3 chondrites as detected by infrared spectroscopy. *Geochimica et Cosmochimica Acta* 75:3530–3541.

Kitazato K., Milliken R.E., Iwata T., Abe M., Ohtake M., Matsuura S., Arai T., Nakauchi Y., Nakamura T., Matsuoka M., Senshu H., Hirata N., Hiroi T., Pilorget C., Brunetto R., Poulet F., Riu L., Bibring J.P., Takir D., Domingue D.L., Vilas F., Barucci M.A., Perna D., Palomba E., Galiano A., Tsumura K., Osawa T., Komatsu M., Nakato A., Arai T., Takato N., Matsunaga T., Takagi Y., Matsumoto K., Kouyama T., Yokota Y., Tatsumi E., Sakatani N., Yamamoto Y., Okada T., Sugita S., Honda R., Morota T., Kameda S., Sawada H., Honda C., Yamada M., Suzuki H., Yoshioka K., Hayakawa M., Ogawa K., Cho Y., Shirai K., Shimaki Y., Hirata N., Yamaguchi A., Ogawa N., Terui F., Yamaguchi T., Takei Y., Saiki T., Nakazawa S., Tanaka S., Yoshikawa M., Watanabe S., and Tsuda Y. 2019. The surface composition of asteroid 162173 Ryugu from Hayabusa2 near-infrared spectroscopy. *Science* 364:272–275.

Lane M. D., Morris R. V., Mertzman S. A., and Christensen P. R. 2002. Evidence for platy hematite grains in Sinus Meridiani, Mars. *Journal of Geophysical Research Atmospheres* 107:5126.

Lauretta D., Bartels A. E., Barucci M. A., Bierhaus E. B., Binzel R. P., Bottke W. F., Campins H., Chesley S. R., Clark B. C., Clark B. E., Cloutis E. A., Connolly H. C., Crombie M. K., Delbó M., Dworkin J. P., Emery J. P., Glavin D. P., Hamilton V. E., Hergenrother C. W., Johnson C. L., Keller L. P., Michel P., Nolan M. C., Sandford S. A., Scheeres D. J., Simon A. A., Sutter B. M., Vokrouhlický D., and Walsh K. J. 2015. The OSIRIS-Rex target asteroid (101955) Bennu: Constraints on its physical, geological, and dynamical nature from astronomical observations. *Meteoritics & Planetary Science* 50:834–849.

Le Guillou C., Bernard S., Brearley A. J., and Remusat L. 2014. Evolution of organic matter in Orgueil, Murchison and Renazzo during parent body aqueous alteration: In situ investigations. *Geochimica et Cosmochimica Acta* 131:368.

Liu Y., Meirer F., Williams P. A., Meirer F., Williams P. A., Wang J., Andrews J. C., and Pianetta P. 2011. TXM-Wizard: A program for advanced data collection and evaluation in full-field transmission X-ray microscopy. *Journal of Synchrotron Radiation* 19:281.

Liu Y., Kiss A. M., Larsson D. H., Yang F., and Pianetta P. 2016. To get the most out of high resolution X-ray tomography: A review of the postreconstruction analysis. *Spectrochimica Acta Part B: Atomic Spectroscopy* 117:29.

Martin M. C., Dabat-Blondeau C., Unger M., Sedlmair J., Parkinson D. Y., Bechtel H. A., Illman B., Castro J. M., Keiluweit M., Buschke D., Ogle B., Nasse M. J., and Hirschmugl C. J. 2013. 3D spectral imaging with synchrotron Fourier transform infrared spectro-microtomography. *Nature Methods* 10:861–864.

Matrajt G., Borg J., Raynal P. I., Djouadi Z., d'Hendecourt L., Flynn G., and Deboffle D. 2004. FTIR and Raman analyses of the Tagish Lake meteorite: Relationship with the aliphatic hydrocarbons observed in the diffuse interstellar medium. *Astronomy & Astrophysics* 416:983–990.

Merouane S., Djouadi Z., D'Hendecourt L., Zanda B., and Borg J. 2012. Hydrocarbon materials of the likely interstellar origin from the Paris meteorite. *The Astrophysical Journal* 756:154–160.

Merouane S., Djouadi Z., and Le Sergeant d'Hendecourt L. 2014. Relations between aliphatics and silicate components in 12 stratospheric particles deduced from vibrational spectroscopy. *The Astrophysical Journal* 780:174–185.

Murata K., Chihara H., Tsuchiyama A., Koike C., and Takakura T. 2007. Crystallization experiments on amorphous silicates with chondritic composition: Quantitative formulation of the crystallization. *The Astrophysical Journal* 668:285–293.

Nakamura T., Noguchi T., Tsuchiyama A., Ushikubo T., Kita N. T., Valley J. W., Zolensky M. E., Kakazu Y., Sakamoto K., Mashio E., Uesugi K., and Nakano T. 2008. Chondrule like objects in short-period comet 81P/Wild 2. *Science* 321:1664–1667.

Nakamura T., Noguchi T., Tanaka M., Zolensky M. e, Kimura M., Tsuchiyama A., Nakato A., Ogami T., Ishida H., Uesugi M., Yada T., Shirai K., Fujimura A., Okazaki R., Sandford S. A., Ishibashi Y., Abe M., Okada T., Ueno M., Mukai T., Yoshikawa M., and Kawaguchi J. 2011. Itokawa dust particles: A direct link between S-type asteroids and ordinary chondrites. *Science* 333:1113–1116.

Nakamura E., Makishima A., Moriguti T., Kobayashi K., Tanaka R., Kunihiro T., Tsujimori T., Sakaguchi C., Kitagawa H., Ota T., Yachi Y., Yada T., Abe M., Fujimura A., Ueno M., Mukai T., Yoshikawa M., and Kawaguchi J. 2012. Space environment of an asteroid preserved on micrograins returned by the Hayabusa spacecraft. *Proceedings of the National Academy of Sciences of the United States of America* 109:624–629.

Nakamura T., Nakato A., Ishida H., Wakita S., Noguchi T., Zolensky M. E., Tanaka M., Kimura M., Tshuchiyama A., Ogami T., Hashimoto T., Konno M., Uesugi M., Yada T., Shirai K., Fujimura A., Okazaki R., Sandford S. A., Ishibashi Y., Abe M., Okada T., Ueno M., and Kawaguchi J. 2014. Mineral chemistry of MUSES-C Regio inferred from analysis of dust particles collected from the first- and second-touchdown sites on asteroid Itokawa. *Meteoritics & Planetary Science* 49:215–227.

Nakashima D., Kita N. T., Ushikubo T., Noguchi T., Nakamura T., and Valley J. W. 2013. Oxygen three-isotope ratios of silicate particles returned from asteroid Itokawa by the Hayabusa spacecraft: A strong link with equilibrated LL-chondrites. *Earth and Planetary Science Letters* 379:127–136.

Noguchi T., Kimura M., Hashimoto T., Konno M., Nakamura T., Zolensky M. E., Tsuchiyama A., Matsumoto T., Matsuno J., Okazaki R., Uesugi M., Karouji Y., Yada T., Ishibashi Y., Shirai K., Abe M., and Okada T. 2014. Sylvite and halite on particles recovered from 25143 Itokawa: A preliminary report. *Meteoritics & Planetary Science* 49:1305.

Omori K. 1971. Analysis of the infrared absorption spectrum of diopsode. *The American Mineralogist* 56:9–10.

Orthous-Daunay F. R., Quirico E., Beck P., Brissaud O., Dartois E., Pino T., and Schmitt B. 2013. Mid-infrared study of the molecular structure variability of insoluble organic matter from primitive chondrites. *Icarus* 223:534–543.

Pendleton Y. J., Sandford S. A., Allamandola L. J., Tielens A. G. G. M., and Sellgren K. 1994. Near-infrared absorption spectroscopy of interstellar hydrocarbon grains. *The Astrophysical Journal* 437:683–696.

Quaroni L., Obst M., Nowak M., and Zobi F. 2015. Three-dimensional mid-infrared tomographic imaging of endogenous and exogenous molecules in a single intact cell with subcellular resolution. *Angewandte Chemie International Edition* 54:318–322.

Rietmeijer F. J. M. 1998. Interplanetary dust particles. In *Planetary materials*, edited by Papike J. J. *Reviews in Mineralogy*, vol. 36. Washington, D.C.: Mineralogical Society of America. pp. 2-01–2-96.

Sandt C., Dionnet Z., Toplak T., Fernandez E., Brunetto R., and Borondics F. 2019. Performance comparison of aperture-less and confocal infrared microscopes. *Journal of Spectral Imaging* 8:a8.

Sears D. W. G., Sears H., Ebel D. S., Wallace S., and Friedrich J. M. 2016. X-ray computed tomography imaging: A not-so-nondestructive technique. *Meteoritics & Planetary Science* 51:833–838.

Sugita S., Honda R., Morota T., Kameda S., Sawada H., Tatsumi E., Yamada M., Honda C., Yokota Y., Kouyama T., Sakatani N., Ogawa K., Suzuki H., Okada T., Namiki N., Tanaka S., Iijima Y., Yoshioka K., Hayakawa M., Cho Y., Matsuoka M., Hirata N., Hirata N., Miyamoto H., Domingue D., Hirabayashi M., Nakamura T., Hiroi T., Michikami T., Michel P., Ballouz R.-L., Barnouin O. S., Ernst C. M., Schröder S. E., Kikuchi H., Hemmi R., Komatsu G., Fukuhara T., Taguchi M., Arai T., Senshu H., Demura H., Ogawa Y., Shimaki Y., Sekiguchi T., Müller T. G., Hagermann A., Mizuno T., Noda H., Matsumoto K., Yamada R., Ishihara Y., Ikeda H., Araki H., Yamamoto K., Abe S., Yoshida F., Higuchi A., Sasaki S., Oshigami S., Tsuruta S., Asari K., Tazawa S., Shizugami M., Kimura J., Otsubo T., Yabuta H., Hasegawa S., Ishiguro M., Tachibana S., Palmer E., Gaskell R., Le Corre L., Jaumann R., Otto K., Schmitz N., Abell P. A., Barucci M. A., Zolensky M. E., Vilas F., Thuillet F., Sugimoto C., Takaki N., Suzuki Y., Kamiyoshihara H., Okada M., Nagata K., Fujimoto M., Yoshikawa M., Yamamoto Y., Shirai K., Noguchi R., Ogawa N., Terui F., Kikuchi S., Yamaguchi T., Oki Y., Takao Y., Takeuchi H., Ono G., Mimasu Y., Yoshikawa K., Takahashi T., Takei Y., Fujii A., Hirose C., Nakazawa S., Hosoda S., Mori O., Shimada T., Soldini S., Iwata T., Abe M., Yano H., Tsukizaki R., Ozaki M., Nishiyama K., Saiki T., Watanabe S., and Tsuda Y. 2019. The geomorphology, color, and thermal properties of Ryugu: Implications for parent-body processes. *Science* 364:230.

Susi H. and Byler D. M. 1983. Protein structure by Fourier transform infrared spectroscopy: Second derivative spectra. *Biochemical and Biophysical Research Communications* 115:391–397.

Takagi Y., Yoshikawa M., Abe M., Tachibana S., Okada T., Kitazato K., Nakamura R., Hirata N., Yano H., Demura H., Nakazawa S., Iijima Y., Shirai K., Hayakawa M., and the Hayabusa 2 Project Team. 2011. Hayabusa 2, C-type asteroid sample return mission. AGU fall meeting.

Takeuchi A., Uesugia K., and Suzukia Y. 2013. Three-dimensional phase-contrast X-ray microtomography with scanning–imaging X-ray microscope optics. *Journal of Synchrotron Radiation* 20:793–800.

Tsuchiyama A., Nakamura T., Okazaki T., Uesugi K., Nakano T., Sakamoto K., Akaki T., Iida Y., Kadono T., Jogo K., and Suzuki Y. 2009. Three-dimensional structures and elemental distributions of Stardust impact tracks using synchrotron microtomography and X-ray fluorescence analysis. *Meteoritics & Planetary Science* 44:1203–1224.

Tsuchiyama A., Uesugi M., Matsushima T., Michikami T., Kadono T., Nakamura T., Uesugi K., Nakano T., Sandford S. a, Noguchi R., Matsumoto T., Matsuno J., Nagano T., Imai Y., Takeuchi A., Suzuki Y., Ogami T., Katagiri J., Ebihara M., Ireland T. r, Kitajima F., Nagao K., Naraoka H., Noguchi T., Okazaki R., Yurimoto H., Zolensky M. E., Mukai T., Abe M., Yada T., Fujimura A., Yoshikawa M., and Kawaguchi J. 2011. Three-dimensional structure of Hayabusa samples: Origin and evolution of Itokawa regolith. *Science* 333:1125–1128.

Tsuchiyama A., Nakano T., Uesugi K., Uesugi M., Takeuchi A., Suzuki Y., Noguchi R., Matsumoto T., Matsuno J., Nagano T., Imai Y., Nakamura T., Ogami T., Noguchi T., Abe M., Yada T., and Fujimura A. 2013. Analytical dual-energy microtomography: A new method for obtaining three-dimensional mineral phase images and its application to Hayabusa samples. *Geochimica et Cosmochimica Acta* 116:5–16.

Tsuchiyama A., Uesugi M., Uesugi K., Nakano T., Noguchi R., Matsumoto T., Matsuno J., Nagano T., Imai Y., Shimada A., Takeuchi A., Suzuki Y., Nakamura T., Noguchi T., Abe M., Yada T., and Fujimura A. 2014. Three-dimensional microstructure of samples recovered from asteroid 25143 Itokawa: Comparison with LL5 and LL6 chondrite particles. *Meteoritics & Planetary Science* 49:172–187.

Tsuchiyama A., Nakano T., Uesugi K., Takeuchi A., and Miyake A. 2016. SR-based analytical micro-nanotomography and its appication to extraterrestrial materials (abstract). *Goldschmidt* 2016:3193.

Vinogradoff V., Le Guillou C., Bernard S., Binet L., Cartigny P., Brearley A. J., and Remusat L. 2017. Paris vs. Murchison: Impact of hydrothermal alteration on organic matter in CM chondrites. *Geochimica et Cosmochimica Acta* 212:234.

Watanabe S., Hirabayashi M., Hirata N., Hirata N., Noguchi R., Shimaki Y., Ikeda H., Tatsumi E., Yoshikawa M.,

Kikuchi S., Yabuta H., Nakamura T., Tachibana S., Ishihara Y., Morota T., Kitazato K., Sakatani N., Matsumoto K., Wada K., Senshu H., Honda C., Michikami T., Takeuchi H., Kouyama T., Honda R., Kameda S., Fuse T., Miyamoto H., Komatsu G., Sugita S., Okada T., Namiki N., Arakawa M., Ishiguro M., Abe M., Gaskell R., Palmer E., Barnouin O. S., Michel P., French A. s, McMahon J. W., Scheeres D. J., Abell P. A., Yamamoto Y., Tanaka S., Shirai K., Matsuoka M., Yamada M., Yokota Y., Suzuki H., Yoshioka K., Cho Y., Tanaka S., Nishikawa N., Sugiyama T., Kikuchi H., Hemmi R., Yamaguchi T., Ogawa N., Ono G., Mimasu Y., Yoshikawa K., Takahashi T., Takei Y., Fujii A., Hirose C., Iwata T., Hayakawa M., Hosoda S., Mori O., Sawada H., Shimada T., Soldini S., Yano H., Tsukizaki R., Ozaki M., Iijima Y., Ogawa K., Fujimoto M., Ho T-m, Moussi A., Jaumann R., Bibring J-P., Krause C., Terui F., Saiki T., Nakazawa S., and Tsuda Y. 2019. Hayabusa2 arrives at the carbonaceous asteroid 162173 Ryugu—A spinning top–shaped rubble pile. *Science* 364:268–272.

Yada T., Fujimara A., Abe M., Nakamura T., Noguchi T., Okazaki R., Nagao K., Ishibashi Y., Shirai K., Zolensky M. E., Sandford S., Okada T., Uesugi M., Karouji Y., Ogawa M., Yakame S., Ueno M., Mukai T., Yoshikawa M., and Kawaguchi J. 2014. Hayabusa-returned sample curation in the Planetary Material Sample Curation Facility of JAXA. *Meteoritics & Planetary Science* 49:135–153.

Yano H., Kubota T., Miyamoto H., Takagi Y., Yoshida K., Abe M., Abe S., Barnouin-Jha O., Fujiwara A., Hasegawa S., Hashimoto T., Ishiguro M., Kato M., Kawaguchi J., Mukai T., Saito J., Sasaki S., and Yoshikawa M. 2006. Touchdown of the Hayabusa Spacecraft at the Muses Sea on Itokawa. *Science* 312:1350–1353.

Yesiltas M. and Kebukawa Y. 2016. Associations of organic matter with minerals in Tagish Lake meteorite via high spatial resolution synchrotron-based FTIR microspectroscopy. *Meteoritics & Planetary Science* 51:584–595.

Yesiltas M., Kebukawa Y., Peale R. E., Mattson E., Hirschmugl C. J., and Jenniskens P. 2014. Infrared imaging spectroscopy with micron resolution of Sutter's Mill meteorite grains. *Meteoritics & Planetary Science* 49:2027–2037.

Yesiltas M., Sedlmair J., Peale R. E., and Hirschmugl C. J. 2016b. Synchrotron-based three-dimensional Fourier-transform infrared spectro-microtomography of Murchison meteorite grain. *Applied Spectroscopy* 71:1198–1208.

Yesiltas M., Jaret S., Young J., Wright S. P., and Glotch T. D. 2018. Three-dimensional Raman tomographic microspectroscopy: A novel imaging technique. *Earth and Space Science* 5:380–392.

Yoshikawa M., Fujiwara A., and Kawaguchi J. 2007. Hayabusa and its adventure around the tiny asteroid Itokawa. *Highlights of Astronomy* 14:323–324.

Yurimoto H., Abe K.-I., Abe M., Ebihara M., Fujimura A., Hashiguchi M., Hashizume K., Ireland T. R., Itoh S., Katayama J., Kato C., Kawaguchi J., Kawasaki N., Kitajima F., Kobayashi S., Meike T., Mukai T., Nagao K., Nakamura T., Naraoka H., Noguchi T., Okazaki R., Park C., Sakamoto N., Seto Y., Takei M., Tsuchiyama A., Uesugi M., Wakaki S., Yada T., Yamamoto K., Yoshikawa M., and Zolensky M. E. 2011. Oxygen isotopic compositions of asteroidal materials returned from Itokawa by Hayabusa mission. *Science* 333:1116–1119.

Zanda B., Bourot-Denise M., Hewins R. H., Barrat J. A., and Gattacceca J. 2010. The Paris CM chondrite yields new insights on the onset of parent body alteration (abstract #5312). *Meteoritics & Planetary Science* 45:5312.

SUPPORTING INFORMATION

Additional supporting information may be found in the online version of this article.

Video S1. 3-D reconstruction of the Paris meteorite fragment obtained with X-CT (gray) and IR tomography. The different functional groups were shown in different colors: light blue for the OH bending, dark blue for the OH stretching, green for the silicates, red for the aliphatic organic matter, and purple for the carbonates.